Toward Sea Ice Monitoring Through Remote Sensing using SAR
OE 560 - Introduction to Remote Sensing

Nathaniel Burgdorfer

Stevens Institute of Technology

Hoboken, New Jersey, USA

nburgdor@stevens.edu

Abstract

Sea ice is an important feature of our environment, contributing to many aspects of our climate and ecosystem. Monitoring sea ice is a difficult and important task. In this work, we aim to review several different methods of monitoring global sea ice. We specifically aim to analyze methods of estimating sea ice thickness [6, 8, 14] and estimating sea ice drift [1, 3] through remote sensing techniques using SAR. We will provide a comprehensive study of both sub-topics, introducing relevant background, technical specifications of equipment, comparisons of the different methods, and further discussions of each estimation task.

1. Introduction

The physical properties of sea ice have a significant impact on the environment, both locally and globally. In this work, we investigate two properties of sea ice: thickness and drift. While there are several physical properties of sea ice that can be monitored, we restrict this discussion to these two in order to provide a detailed analysis of how remote sensing techniques through Synthetic Aperture Radar (SAR) can be utilized to monitor sea ice.

The influence of sea ice thickness (SIT) on the ecosystem can have many environmental factors. One of which is the salinity of the water underneath the ice. This can influence the air-ice and ice-water fluxes, affecting temperature and moisture, as well as ocean currents and circulation. Thick sea ice is also an important ocean insulator, reflecting much of the radiation from the sun and preventing the absorption of energy.

Sea ice (especially thick sea ice) also provides many marine species with a habitable environment. Ice along the shores in marginal regions can help protect coastlines from erosion due to weather and storm surges. Ice over sea water can also help to trap carbon dioxide and other air pollutants that aid in global warming.

Similar to SIT, sea ice drift also greatly impacts the environment. Locally, sea ice drift can cause disturbances as ice moves away from local animal habitats. This can displaces these species, ultimately affecting the overall predatory hierarchy of the Arctic and surrounding environments. Drift in sea ice, similar to thickness, can affect the ability of the oceans to store carbon dioxide and other air pollutants, which can greatly impact the temperature of the global atmosphere. The local availability of resources is also impacted by ice drift, with potential changes in wind currents, ocean salinity, and water temperature.

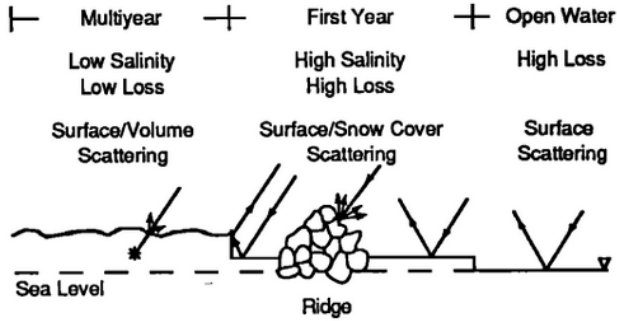Drifting sea ice can have substantial impacts on local enterprises. Relying on navigating around

1

Figure 1. Depiction of the backscattering interaction with First-Year Ice (FYI), Multi-Year Ice (MYI), and open water [13].

large sections of sea ice, shipping lanes and transportation can directly be affected, which can result in an increase in shipping costs, supply chain, and overall dangerous transport conditions. These dangers are also extended into the fishing industry, affecting the availability and safety of local fishing. Furthermore, comparative to thin sea ice on coastlines, ice drift can cause erosion along the shore, which has the potential to damage infrastructure and negatively impact coastal ecosystems.

Monitoring sea ice properties, such as sea ice thickness and sea ice drift, can aid researchers in understanding the overall environmental state of both the Arctic regions, as well as the global environment. Sea ice is a major contributor to the regulation of energy that is exchanged between the atmosphere and the ocean. It acts as both a temperature insulator, as well as a physical dampening system against large wave action and currents. With much of the marine transportation and aquaculture industries negatively affected by sea ice, it is important to be able to accurately monitor and estimate sea ice properties. Understanding these properties can provide insight into the state of the overall environment, regional environment, and effects this might have on local and global ecosystems.

2. Background

2.1. Sea Ice stages

There are several stages of ice formation, each of which having different physical properties affecting remote sensing techniques [13]. The main stages of ice formation include:

- Open Water

- First-Year Ice (FYI)

- Multi-Year Ice (MYI)

There can also be a subcategory of MYI labeled *Second-Year Ice*; however, we use the overall stage of MYI to refer to this subcategory (see Figure 1 for a depiction of backscattering based on ice stage). Both open water and FYI are high loss stages, in which much of the backscatter energy is determined by the surface roughness of the ice (or water). In contrast to these high loss stages, backscatter from MYI is dependent on both surface and volume scattering. MYI is not only thicker than FYI, but also contains less salinity and potentially more air pockets, allowing radiation to penetrate deeper into the material and produce volume scattering. MYI tends to also have more snow cover in part from the fact that MYI does not melt during warmer months. The snow cover can also act as an insulator from solar radiation, aiding in the prevention of melting.

2.2. Dielectric constant

An important term that must be mentioned is the dielectric constant (also known as relative permittivity). The dielectric constant is a characteristic of a material that describes the material ability to store electric energy. When attempting to obtain information on the physical properties of sea ice (in this study, thickness and drift) through remote sensing techniques, it is important to take into account the chemical properties of sea ice and how they correlate with physical properties. Probing sea ice with electromagnetic

energy is affected by permittivity characteristics, causing affects in the propagation and scattering (especially volume scattering) of electromagnetic waves. Several works aim to leverage the knowledge of the dielectric constant of sea ice in order to make connection between the type of ice, as well as perform inference on the sea ice characteristics.

3. Sensors for Sea Information Retrieval

3.1. Sensing Techniques

Ship and In-Situ Observations Manual recording of ice conditions, as well as in-situ ice observations, had been and are still used to record properties of sea ice [16]. Such ship logging is difficult to use as there is no real standardized method for recording ice property information. It is also a challenge to cross-reference many different observations logs written by different individuals into a unified data collection. In-situ observations give much more detailed information of the ice structure. This involves drilling into ice sheets and inspecting the cores. Properties such as thickness, age, salinity, composition, and structure can be observed from ice cores, but the drilling process is time-consuming, expensive, and often difficult to physically perform. They also provide very limited coverage of sea ice sheets, providing small samples that may not be representative of a large spatial area.

Remote Sensing Remote sensing is a useful and practical technique to obtain information from large areas, especially remote locations that are difficult to navigate. Radar is a type of remote sensing technology that uses electromagnetic waves to detect and measure the properties of objects. Radar sends out short pulses of radio waves in a specific directing in order to probe the surrounding environment. These radio waves bounce off of object in front of the radar and return responses back to the system antenna. These responses are received by the radar and are interpreted based on several properties of the returning wave (frequency, amplitude, intensity, time-of-flight). Radar is typically not used in sea ice monitoring, as this is mainly nadir-facing and holds ambiguities of reflectance from an undetermined point on the surface (surface snow, ice, open water, etc.) [16]. Instead, the synthetic aperture radar (SAR) is the remote sensing tool of choice for information retrieval in the arctic regions.

3.2. Principles of Synthetic Aperture Radar (SAR)

Synthetic Aperture Radar (SAR) is a type of radar system that transmits electromagnetic waves into the environment in order to measure backscattering and deduce material structures, characteristics, and distances. SAR makes use of several different observations taken at different time-steps in order to construct an analogous sensing modality similar to a radar with a very large aperture. This property of simulating a large aperture through a geometric time-delay leads to much higher spatial resolutions. SAR typically operates in X-, C-, or L- band under the following frequencies:

- X-band: 8-12 GHz

- C-band: 4-8 GHz

- L-band: 1-2 GHz

SAR uses the backscattering information collected from the environment to construct an image of the mapped region of interest. It can operate in all-weather conditions, and during the night (similar to other active sensors). This make SARs very desirable for continuous mapping of environments like the Arctic.

3.3. SAR Polarization

Polarization is an important feature of radar. Polarization refers to the plane orientation of the transmitted and received waves. The waves oscillate in specific planes and depending on the specified transmit and receive path, SARs can
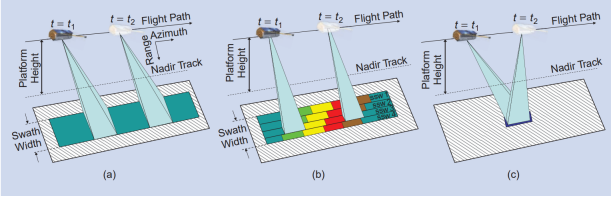
Figure 2. Depiction of the different scanning modes for Synthetic Aperture Radar [10]. (a) shows an SAR in Strip-Map mode, (b) shows an SAR in ScanSAR mode, and (c) shows an SAR in Spotlight mode.

detect different backscattering patterns from surfaces and objects. Typically, SARs transmit and receive these waves in linear polarizations, in which they either specify a horizontal plane, denoted by H, or a vertical plane, denoted by V. When the polarization is specified as HH, this indicates that it transmits and receives electromagnetic waves in the horizontal plane orientation. If it is specified that the polarization is VH, the SAR transmits waves in vertical orientation and receives signals in the horizontal plane. Different polarization orientations can lead to identifying different surface properties. Certain polarization combinations may be used to detecting volume scattering backscatter better, while another may be more suited to identify rough surface conditions. We will see that many of the works presented in this paper utilize different (and sometimes multiple) polarization configurations.

3.4. SAR Modes

There are several different modes of SAR, each with its own advantages and disadvantages:

- Strip-Map Mode

- Spotlight Mode

- ScanSAR Mode

Strip-Map mode is a mode in which the antenna of the SAR remains in a fixed position throughout the flight. This is usually fixed along the path of travel of the airborne SAR, with potentially a slight tilt forward or backward.

Spotlight mode is a scan pattern in which the SAR focuses the antenna on a small region. The antenna stays fixed on this spotlight region while passing overhead. This allows for high resolution scanning of the desired location, but results in a very small scanning coverage.

ScanSAR mode is when the SAR antenna sweeps periodically and covers a much larger area. With this mode, there is a trade-off between azimuth resolution and the size of the area that is being mapped. The larger the sweeping area, the worse the azimuth resolution. Figure 2 shows examples of the different scanning modes.

4. Estimating Sea Ice Parameters

In the following section, we will explore several different methods for detecting the thickness and drift of sea ice. We use these two characteristics as a proxy to study the affects that different SAR scanning modes, polarizations, and multimodal sensing inputs have on the inference of sea ice properties. We first analyze a few methods of estimating sea ice thickness, followed by an overview of several methods to estimate sea ice drift. We will then provide some discussion on the articles presented here, with in-site on potential research directions.

4.1. Sea Ice Thickness (SIT)

Article 1. The work by Shi et al. named *Sea Ice Thickness Retrieval From SAR Imagery Over the Bohai Sea* [14] builds off of work done by Karvonen et al. [5], and use a hybrid method for detecting the thickness of observed sea ice. This work applies a numerical sea ice model alongside SAR imagery. They use 10 ScanSAR wide mode RADARSAT-2 images with HH/HV dual-polarization operating at C-band with a center frequency of 5.405 GHz. The spatial resolution of the SAR images is roughly 3 - 100 meters, with a swath width of 500km and a pixel spacing of about 50m. The thermodynamic model used in this research is the *high-resolution thermodynamic snow and ice (HIGHTSI)* model. The
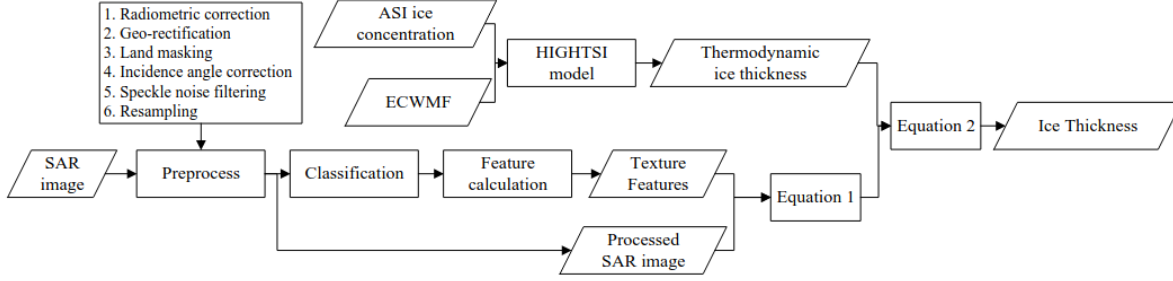
Figure 3. Algorithm pipeline [14].

model was originally introduced to explore ice and snow thermodynamics in seasonally covered areas, but has been adapted to analyzing areas with year-round sea coverage. The model looks to compute heat conductivity for multi-layered snow and ice coverage, modeling thickness and thermodynamics of these layers. Many parameters are considered in the model: solar radiation, air-ice fluxes, ice color and albedo, cloud cover, and subsurface snow and ice melting. The input atmospheric forcing information is taken from the *European Centre for Medium-Range Weather Forecasts (ECMWF)*. The model also uses the daily ice concentrations computed from the *Artist Sea Ice (ASI)* algorithm using data from the *Advanced Microwave Scanning Radiometer 2 (AMSR2)* [15] to produce the thermodynamic estimate of ice thickness. This thermodynamic estimate is used as a prior for the SAR imagery to aid in the estimation of sea ice thickness. Before the SAR data can be used in an estimation pipeline, the data must be pre-processed. The first processing step is a calibration, or in other words, a radiometric correction of the SAR images to obtain the logarithmic backsacattering coefficients σ^0, which are denoted in decibels, using the following calibration equations [5],

$$\sigma^0 = \frac{A^2}{K}sin(\alpha) = \frac{I}{K}sin(\alpha) \quad (1)$$
$$\sigma^0(dB) = 10log_{10}(\sigma^0) \quad (2)$$

where A is the amplitude value, K is the calibration coefficient, α is the incidence angle, and I is the intensity for the SAR. In practice, the incidence angle ranges from $20°$ to $50°$. After geo-rectification (following LCC projection [17]) and land masking [21], the SAR images are processed to correct the incidence angle and pass through a speckle noise filtering stage in order to produce the final SAR image mosaic of the desired area (see Figure 4).

With the processed SAR images, Shi et al. run k-means clustering on the SAR image in order to segment the images into groups of similar backscattering coefficients. K-Means clustering is an algorithm commonly found in Computer Vision literature, although its origin is from the signal processing community [9]. Two texture (pattern) features of the images are then computed from this segmentation: the number of edge pixels relative to segment area, and the ratio of the standard-deviation to the mean of the backscattering coefficient, per-segment. We leave much of the details of these image processing stages as an exercise for the reader as image processing is mostly out of scope for this work.

In evaluating the feature choices, the authors choose to exclude the first texture feature (the number of edge pixels relative to the segment area) after looking at the correlations between this feature and in-situ ice thickness measurements. The pre-processed SAR image and the second feature were used to estimate ice thickness through a linear model. Then another linear model was used incorporating the output of the HIGHTSI model and the SAR data to produce the
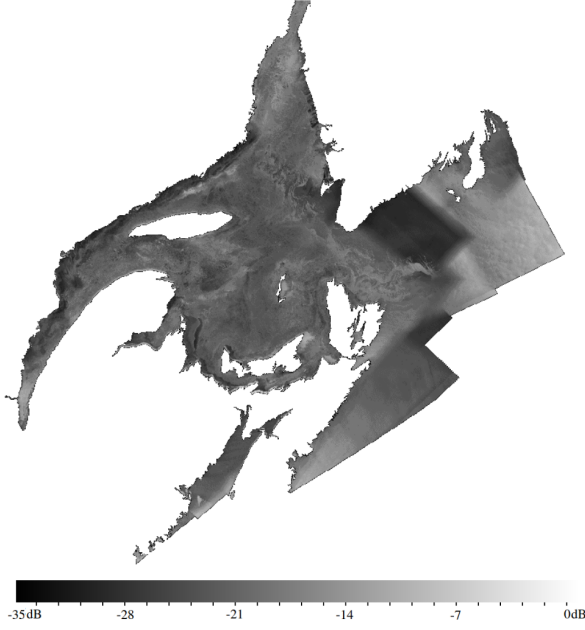
5

Figure 4. SAR mosaic after processing (shown in dB scale) of the Gulf of St. Lawrence off Canada [5].

final estimate of ice thickness, H,

$$H_1 = 1.321\sigma^0 - 258.8F_2 + 21.93 \qquad (3)$$

$$H = 0.4H_1 + 0.6H_{HIGHTSI} \qquad (4)$$

with the overall equation simplifying to,

$$H = 0.5285\sigma^0 - 103.52F_2 + 0.6H_{HIGHTSI} + 8.772 \qquad (5)$$

where σ^0 is the processed backscattering coefficient, F_2 is the second texture feature (the statistics ratio), and $H_{HIGHTSI}$ is the thermodynamic model estimate of ice thickness from the HIGH-TSI model. The entire estimation pipeline can be viewed in Figure 3.

The proposed method works in general, but there is one major issue. The estimation of the thickness of sea ice in marginal regions along the coast (transition regions between sea ice and open sea water) proves to be challenging. The SAR backscattering data for thin ice in these regions is quite similar to the coefficients observed for thick
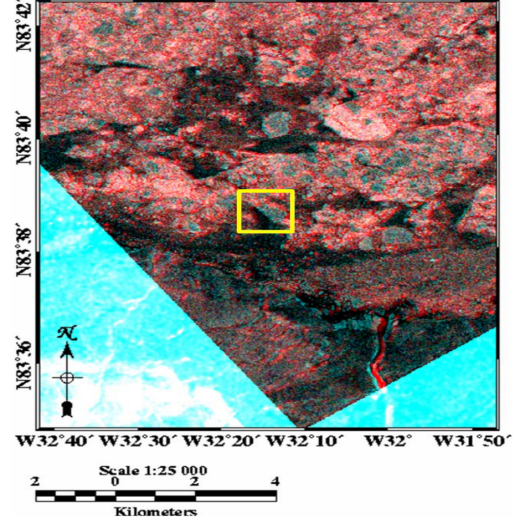

Figure 5. Colorization of sensor images ($\{HV, HH, VV\} \rightarrow \{R, G, B\}$) [6].
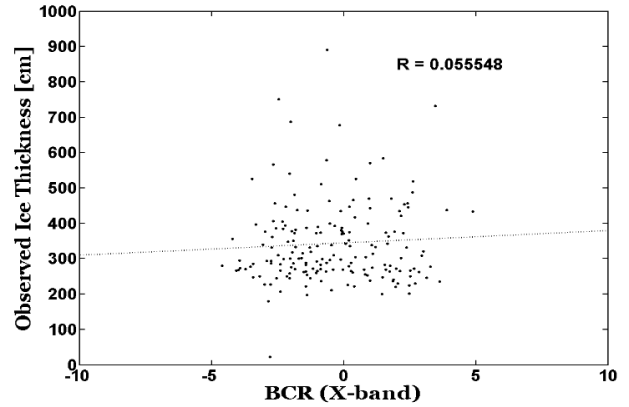

Figure 6. Backscattering coefficient ration (BCR) vs. Ice thickness [6].

ice. This leads to ambiguities in the estimation, and inconsistencies in regions of thin, marginal ice.

Article 2. The work of Kim et al. titled *Es-*

	TerraSAR-X	RADARSAT-2
Date	2009.5.02	2009.4.28
Frequency	9.65GHz (X-band)	5.405GHz (C-band)
Polarization	HH & VV	HH & HV
Incident angle	$27.28° - 29.03°$	$33.61° - 39.75°$

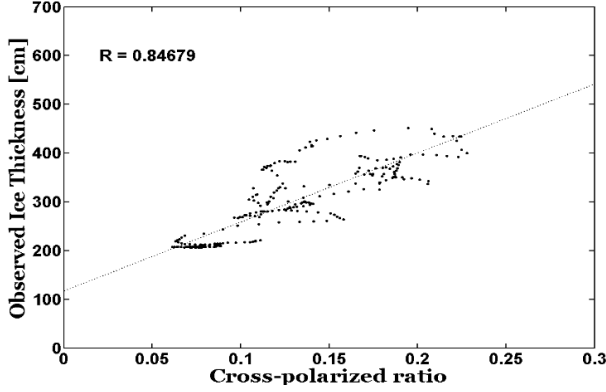Table 1. Equipment specifications used in experiments [6].

6

Figure 7. Cross-polarization ratio vs. Ice thickness [6].

timation of Sea Ice Thickness in the Arctic Sea Using Polarimetric Parameters of C- and X-band Space-Borne SAR Data [6] aim to leverage the relationship between depolarization factors and the physical parameters of sea ice in order to estimate sea ice thickness. Previous work [11, 12, 20] had shown how the cross-polarization ratio (VV-HH) of the backscattering coefficient can be correlated to the thickness of First-Year Ice (FYI), effectively removing the effects of ice surface roughness from the SAR measurements. Kim et al [6] aim to explore the correlation between the cross-polarization ratio from multiple frequency bands of SAR and different physical properties of sea ice to help alleviate the effects of these physical properties during the estimation of sea ice thickness.

They specifically investigate the effects relative to thick FYI and MYI, which were not considered in previous work. To perform their research, the authors used data from TerraSAR-X and RADARSAT-2. TerraSAR-X collected dual-polarization data using VV and HH polarization in Strip Map mode. RADARSAT-2 collected dual-polarization data using HH and HV polarizations in Standard Mode. The specifics of the SAR data collection can be seen in Table 1. Similar image processing to the previous method was used, including radiometric calibration and speckle noise filtering. A colorized depiction of the backscattering coefficients relative to the po-

larization can be viewed in Figure 5.

This work makes use of the extended Bragg scattering model. Essentially, in order to estimate the cross-polarization ratio, the cross-polarization energy of the Bragg surface is converted into a covariance matrix. The definition the authors use is as follows,

$$|R_{HVHH}| = \frac{|S_{HV}|^2}{|S_{HH}|^2} \tag{6}$$

Where R_{HVHH} is the cross-polarization ratio, and S_{HV} and S_{HH} are the polarimetric scattering matrices for the polarization modes of HV and HH, respectively. These matrices depend entirely on the backscatter amplitude of the SAR data (representing the surface roughness information), the incidence angle, and the complex permittivity (which is a property of dielectric materials correlating to the amount of energy absorption of the sea ice),

$$[S] = \begin{bmatrix} S_{HH} & S_{HV} \\ S_{VH} & S_{VV} \end{bmatrix} = m_s \begin{bmatrix} R_S(\theta, \epsilon) & 0 \\ 0 & R_P(\theta, \epsilon) \end{bmatrix} \tag{7}$$

where m_s is the amplitude of the backscatter, and R_S and R_P are the Bragg scattering coefficients of the incidence plane,

$$R_S = \frac{cos\theta - \sqrt{\epsilon - sin^2\theta}}{cos\theta + \sqrt{\epsilon - sin^2 0}} \tag{8}$$

$$R_P = \frac{(\epsilon - 1)(sin^2 0 - \epsilon(1 + sin^2 0))}{(\epsilon cos\theta + \sqrt{\epsilon - sin^2 0})^2} \tag{9}$$

where ϵ is the complex permittivity and θ is the incidence angle. For more information on these formulations, please refer to the work of Hajnsek et al. [2].

Using the X-band data from the TerraSAR-X and the C-band data from the RADARSAT-2, the authors analyze the previously established relationship between the backscatter coefficient ratio (BCR) of VV to HH polarization to sea ice thickness; however, investigating areas with thick

FYI and MYI, which was previously left out of the correlation analysis. In Figure 6, the two data points can be shown to actually have little correlation, with a correlation coefficient of 0.055548. Now, using the C-band data as well as the cross-polarization formulation defined above, the correlation between this value and the thickness of thick FYI and MYI is now much higher, with a correlation coefficient of 0.84679, as shown in Figure 7.

It is observed that the cross-polarization used in this work is sensitive to the surface roughness of the sea ice, and not the dielectric constant. An extended Bragg scattering is used to aid in this analysis, which can allow the estimation of sea ice thickness under the assumption that surface roughness corresponds to SIT.

Article 3. The work of Liu et al. titled *Estimation Of Sea Ice Thickness In The Bohai Sea Using A Combination Of VIS/NIR And SAR Images* [8] explores the multi-modal fusion of VIS/NIR images and SAR images in order to estimate the thickness for sea ice with different levels of surface roughness. SAR data collected for ice with smooth, level surface is not useful for estimating ice thickness due to high reflectivity and low backscattering energy. Ice with this characteristic would be better suited for thickness estimation from VIS/NIR images. On the other hand, VIS/NIR remote sensing is less sensitive to the measurement of sea ice with a rough surface, due to radiative transfer properties [18]. In this case, SAR images would be the preferred data type for estimating ice thickness. This article aims to combine the strengths of each sensing method in order to formulate a complete estimation framework that integrates the effective sensing capabilities of both modalities.

For the VIS/NIR sensing data, Liu et al use the HJ-1 (A/B) satellite. This satellite uses a charge-coupled device (CCD), which is an integrated circuit with an array of linked capacitors used for image sensing. The satellite is also equipped with: (HJ-1A) a Hyper-spectral Imager (HSI), and (HJ-

1B) an IRS infrared sensor. For this work, the authors use the image data taken from the CCD sensor onboard HJ-1B. The CCD sensor holds the following specifications:

- surface spatial resolution: $30m$

- swath width: $360km$

- solar elevation: $33.81°$

- azimuth angle: $343.30°$

- wavelength range (across all bands): $0.43\mu m - 0.90\mu m$

The SAR data that was used in these experiments were pulled from the ENVISAT satellite. The SAR data was captured using with a C-band imaging waveband with several polarization modes: VV, HH, VV/HH, HV/HH, VH/VV. However, for the experiments in this paper, only the VV polarization data is used. The additional specifications are as follows:

- surface spatial resolution: $150m$ (re-sampled to $75m$)

- swath width: $400km$

- solar elevation: $33.81°$

- incidence angle: $19° - 40°$

Because the CCD sensor is obtaining reflective information passively through the atmosphere, in order to work with the VIS/NIR CCD data, an atmospheric correction must be made. The atmospheric reflectance is first computed as follows:

$$\rho^*(\lambda) = \rho_{r+a} + \frac{\rho(\lambda)}{1 - \rho(\lambda)S(\lambda)} T_U(\lambda)T_D(\lambda) \quad (10)$$

where ρ_{r+a} is the reflectance from the atmosphere back towards the satellite, $\rho(\lambda)$ is the surface reflectance, λ is the wavelength, $T_U(\lambda)$ and $T_D(\lambda)$ are the upward and downward atmospheric
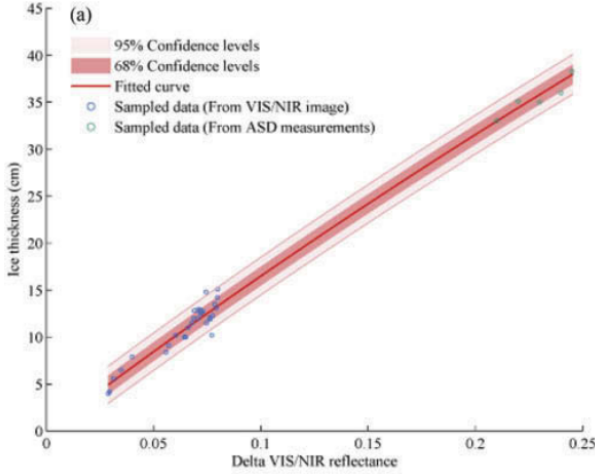
Figure 8. Fitted curve for the relationship between ice thickness and VIS/NIR reflectance [8].

Figure 9. Fitted curve for the relationship between ice thickness and SAR backscattering coefficient [8].

transmittance, and $S(\lambda)$ is the hemispherical reflectance. For more details on computing these terms, please refer to the work of Vermote [19]. With the atmospheric reflectance computed, the surface reflectance is obtained through the following formulation:

$$C = \frac{\rho^*(\lambda) - \rho_{r+a}(\lambda)}{T_U(\lambda)T_D(\lambda)} \qquad (11)$$

$$\rho(\lambda) = \frac{C}{1 + CS(\lambda)} \qquad (12)$$

where $\rho(\lambda)$ is the final corrected surface reflectance.

To utilize the SAR data, the ENVISAT data must also be processed and converted into the corresponding backscattering coefficients,

$$\sigma^{VV} = \frac{DN^2}{K} sin(\alpha) \qquad (13)$$

where, σ^{VV} is the backscattering coefficient, DN is the digital number for each pixel in the SAR image, K is the calibration number, and α is the incidence angle. Similar post-processing of this image is performed, such as the filtering of speckle noise.

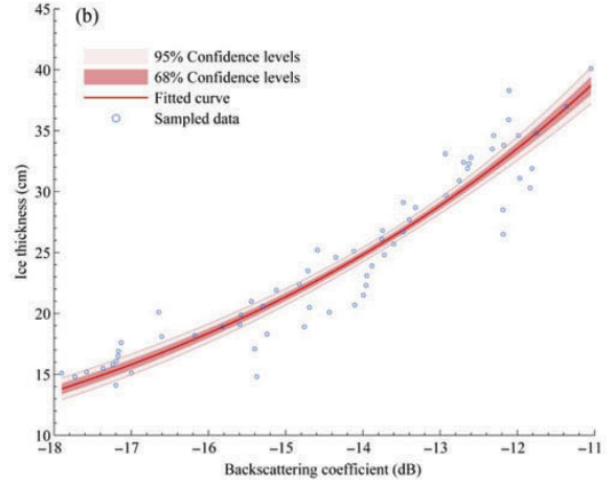To evaluate the correlation between the reflectance from the VIS/NIR images and the backscattering from the SAR data, the relationship between in-situ thickness measurements and these terms was plotted. In Figure 8, we observe the trend between the reflectance and sea ice thickness (with the top-right five points on the curve representing in-situ measurements of thickness vs. reflectance measure with a spectroradiometer at ground level). The curve fitted is logarithmic, and is defined as the following,

$$h_L = 319.5 \ln(1 + \Delta\rho_{VIS/NIR}) \qquad (14)$$

The R^2 (quantifying the goodness of fit for the fitted curve) is $R^2 = 0.988$ (higher is better), with an $RMSE = 0.978$ cm (lower is better). We can observe that the measurements taken at ground-level follow the curve more closely than the samples taken from the HJ-1 satellite. This is most likely a factor of the atmospheric corrections used in the correction of the reflectance term, although the curve fits the data rather well.

In Figure 9, we observe the fitted curve between the sea ice thickness and the SAR backscattering coefficient. The curve fitting here is exponential and is defined as follows:

$$h_R = 203.8 \exp(0.1504\sigma^{VV}) \qquad (15)$$

The R^2 value for this data is $R^2 = 0.90$, with

9

an $RMSE = 2.3$ cm. As we can see from the plots as well as the quantitative curve fitting statistics, the SAR data follows this exponential trend in relation to the sea ice thickness, although more loosely than the VIS/NIR imagery.

This work also makes several assumptions, one of which being the reflective properties of sea ice. This work applies the assumption that the surface exhibits isotropic reflection patterns, since not enough image data was captured at varying angles. This assumption, however does not hold [4] and is baked into the computation of the surface reflectance, potentially resulting in inaccuracies for this term. Another issue that the authors run into is the ability to segment the captured remote sensing maps into land and sea regions. Since both sensing techniques hold some ambiguities attempting to distinguish these two regions, the authors apply a computed mask of the known land area to the captured sensing data. A means of automating this information could be obtained through a prior mapping of the region during warmer months, in which the border between sea and land more obtainable. This would, however, not be a viable option if much of the surrounding sea is still frozen during warmer months.

4.2. Sea Ice Drift

Article 1. Howell et al. aim to analyze and compare the use of L- and C-band SAR estimates and their effectiveness at detecting ice motion vectors over different types of sea ice in their work titled *Comparing L- and C-Band Synthetic Aperture Radar Estimates of Sea Ice Motion Over Different Ice Regimes* [3]. The data used for this work was provided by several different satellites using synthetic aperture radar. The SAR imagery obtained for this research was taken from the RADARSAT-2, PALSAR-1, and PALSAR-2 satellites. The RADARSAT-2 has a 50 m spatial resolution and captured data in ScanSAR mode. The frequency used on this satellite is a 5.405 GHz C-band frequency profile, with the choice of

using only the HH polarization. The PALSAR-1 and PALSAR-2 satellites operate with a spatial resolution of 100 m and 25 m, respectively, also operating in ScanSAR mode. Both satellites operate in L-band, with PALSAR-1 operating with a frequency of 1.270 GHz and PALSAR-2 operating with a frequency of 1.2575 GHz. HH polarization was also used for these satellites. While other polarization configurations are available for these satellites (HV,VV,VH), the choice of HH polarization was based on a lack of information from the PALSAR-1/2 satellites in other polarization configurations, as well as supposed image corruption under the other settings.

To aid in the process of drift vector estimation, determining the ice type and melt stage can be beneficial. To estimate these auxiliary properties, the Advanced Scatterometer (ASCAT) data was used from the European Space Agency's Meteorological Operational (MetOp) satellite. ASCAT (real aperture radar) has a spatial resolution of 25 km; however, the Scatterometer Image Reconstruction (SIR) processing increases the resolution to 4.45 km. The ASCAT operates under VV polarization in C-band with a frequency of 5.255 GHz and an incidence angle of $40°$. Additional data provided by the Canadian Ice Service Digital Archive (CISDA) was also employed.

In order to perform the comparison between L- and C-band SAR data, an ice motion tracking algorithm, developed by Komarov and Barber [7], was used with both data types. The algorithm first applies several layers of image processing, including ice feature identification (through a measure of local SAR image variance), with Gaussian and Laplace operators convolved over the processed images. Phase-correlation and cross-correlation techniques (typically used in feature matching algorithms) are used in tandem in a cycle consistent manner, where the motion vectors are estimated both forward (from image 1 to image 2) and backward (from image 2 to image 1). For further information on the ice motion tracking algorithm, as well as an evaluation of the algo-
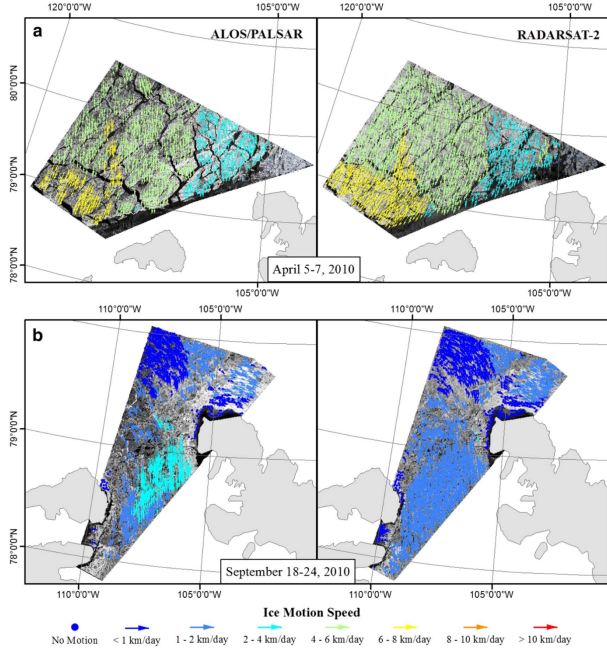
Figure 10. Motion vector fields for L- and C-band SAR under dry MYI conditions [3].
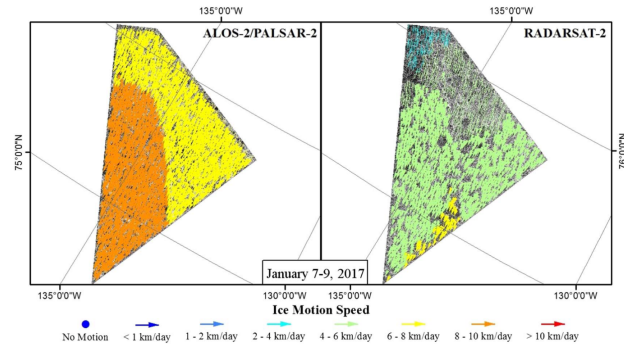

Figure 11. Motion vector fields for L- and C-band SAR under dry FYI conditions [3].

Figure 12. Motion vector fields for L- and C-band SAR under early melt MYI conditions [3].

rithm, we refer the reader to the original paper [7].

The first ice stage evaluated between the different band data is *Dry MYI*. Figure 10 shows the vector fields for the estimated ice tracking for both frequency ranges. For this condition of ice, C-band data from RADARSAT-2 is more sensitive to the thin ice that can be found between ice sheets, leading to more motion vectors and a more continuous motion field. The L-band data is not as sensitive in these areas, producing much less texture (if any) in the regions between ice sheets. Aside from the number of motion vectors, a cross-correlation score, essentially measuring the motion vector quality, is also measured. The cross-correlations for the L-band data were actually higher than the C-band data. Because of the lower frequencies of the L-band SAR, the electromagnetic waves can penetrate further into the thicker MYI sheets, causing high volume scattering and more textures in the SAR images to perform feature matching across images.

The next stage is *Dry FYI*. Figure 11 shows the vector field for this sea ice condition. In this sce-

nario, the L-band data had both a larger number of motion vectors as well as much better quality of vectors, via much larger cross-correlations. The lower frequency L-band with deeper penetrating EM waves is less sensitive to surface scattering of FYI, and is instead quite sensitive to the dielectric properties of the ice and the volume scattering effects of air bubbles. This creates a much more detailed and textured SAR image, allowing for much more accurate feature matching across images, and hence, higher quality ice drift estimation.

Melting conditions are explored next, investigating *MYI under early and advanced melt*. Figure 12 and Figure 13 show the motion vector fields for the early melt MYI and advanced melt MYI, respectively. Again, we can observe the L-band vector fields having an increased density
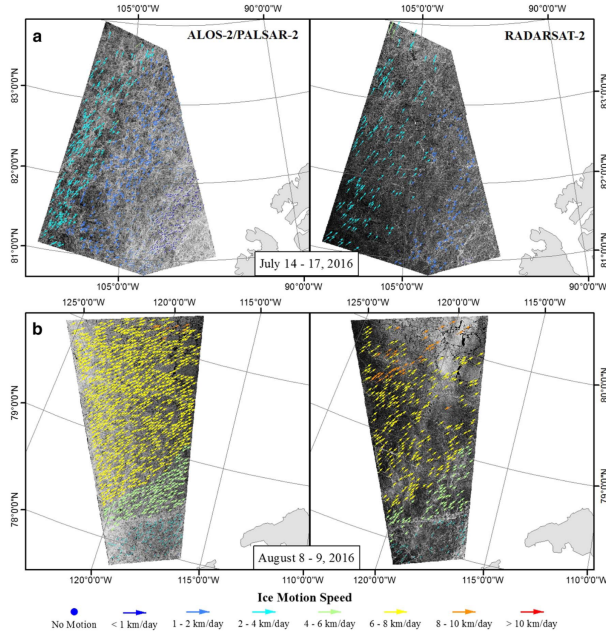
Figure 13. Motion vector fields for L- and C-band SAR under advanced melt MYI conditions [3].

Figure 14. Motion vector fields for L- and C-band SAR under new and grey white ice conditions [3].

of the C-band motion fields. The wet layer of snow and water provide challenges for higher frequency C-band waves, with increased absorption and lower wave penetration. The L-band waves are able to penetrate the wet surface and into the ice, resulting in much higher details in the SAR backscatter images. This results in a larger number of high quality motion vectors.

The final stage observed is *new and grey white ice*. Figure 14 shows the vector field for this stage of ice formation. This newly formed (or in the process of forming) ice exhibits a thinner structure, with an increase in surface roughness during formation. Because of these characteristics, L-band is again much more effective at detecting highly detailed texture features of the sea ice. The surface roughness negatively affects C-band SAR, with the L-band benefiting from detecting the deeper, ice-water boundary, which can be highly detailed. The vector fields fro the L-band contain more motion vectors than the C-band field, as well as higher quality vectors with higher cross-correlation scores.
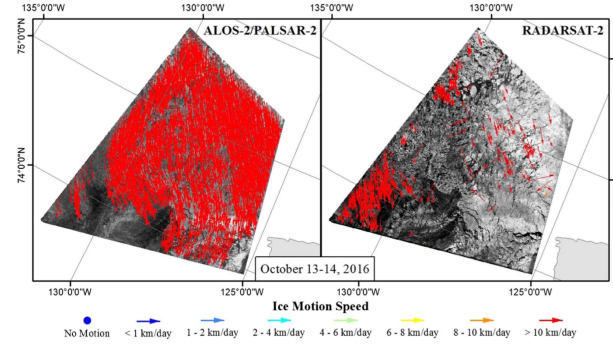
This work looked to quantify previous theoretical assumptions about the potential benefits of using L-band SAR to detect sea ice drift. With a full suit of comprehensive tests over several data samples, comparing L- and C-band SAR in different ice stages and varying thermodynamic states, Howell et al. show just how effective L-band SAR can be at identifying details in sea ice.

Article 2. The work *Enhanced Arctic Sea Ice Drift Estimation Merging Radiometer and Scatterometer Data* [1] by Girard-Ardhuin et al. is intended as a method to join scatterometer and radiometer data into a unified drift field, as opposed to using a single sensing modality. The authors aim to combine a passive sensing Special Sensor Microwave Imager (SSM/I) with backscatter data collected from the SeaWinds/QuikSCAT scatterometer in order to estimate Arctic sea ice drift.

The passive sensors used in this work includes the SSM/I and Advanced Microwave Scanning Radiometer-Earth (AMSR-E). The SSM/I has a spatial resolution of 12.5 km while using the 85.5 GHz channel. Both H and V polarizations are used for these experiments. The AMSR-E has a spatial resolution of 6.25 km when using the 89 GHz channel. Both H and V polarizations are used for this sensor as well.

The active scatterometers used in this work are the SeaWinds/QuikSCAT scatterometer, operating in the Ku-band, and the ASCAT operating in

C-band. The SeaWinds/QuikSCAT utilizes an inner and outer beam sensing structure, in which the inner beam operates at H polarization with a $46°$ incidence angle, and the outer beam operates in V polarization with a $54°$ incidence angle. The backscatter images have a spatial resolution of 12.5 km. The ASCAT uses V polarization and has incidence angle ranging from $25°$ to $65°$. The spatial resolution of the backscatter images is 12.5 km.

Girard-Ardhuin et al. first present the details of the single sensor estimation process before providing a detailed explaination of the fusion process. Estimating a motion vector field from passive sensors can be somewhat limited (based on weather and time-of-year), as this passive sensor requires clear atmospheric conditions and stable radiation. In order to measure displacements and produce motion vectors for the sea ice, the authors employ the maximum cross-correlation (MCC) score between images. The images are first pre-processed, similar to previous methods, by applying Laplacian filtering and smoothing. Following smoothing, the MCC between time-delayed images is computed, producing the raw correlation scores. These scores are then filtered by thresholded an outlier removal method, as well as a local consistency constrained filtering. The active sensor maps are also processed using the same pipeline. The QuikSCAT and ASCAT pre-processed backscattering images, as well as the pre-processed correlations from the passive sensors, are then used to directly infer the drift vector fields.

With the individual drift maps estimated from each modality, The authors aim to combine these estimates to form a complete and complimentary vector field of the sea ice. There are several cases when overlaying the individual vector fields. From the three modalities, there is a maximum possible number of three overlapping drift vectors. See Figure 15 for a depiction of the different states for a drift vector. In situations where multiple drift vectors from the different sources
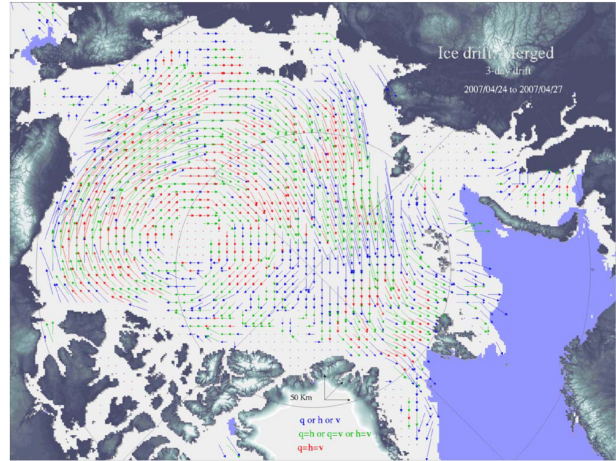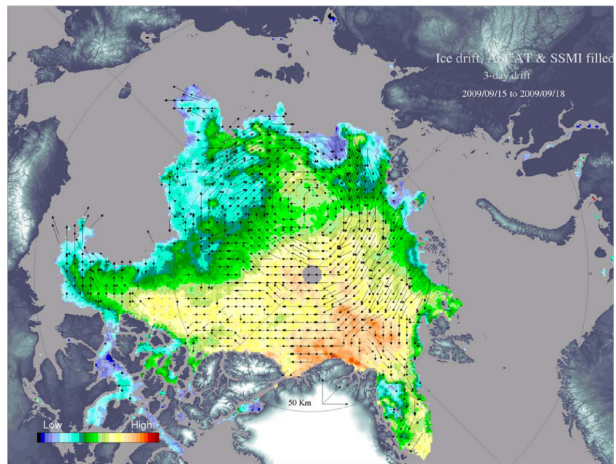

Figure 15. Merged map of drift vectors [1].

Figure 16. Three day ice drift vector field [1].

are overlayed, the authors use a weighted combination scheme to select the appropriate motion vector.

Quantifying the benefits of merging radiometer and scatterometer drift maps, the vector density is computed. Initially, the separate modalities observed low vector densities of $15\% - 60\%$, especially during warm months where radiometer data is unreliable. Combining the sensing techniques leads to density increases to more than 60% density, rising to $80\% - 90\%$ during winter months without a degradation in vector quality.

5. Discussions and Conclusion

The estimation of sea ice thickness and drift come with many challenges. The work presented in this review shows promising results and accurate estimation, but experienced some challenges in different regions under observation. It could be beneficial to include different modalities of remote sensing to aid in particular cases where SARs struggle. Fusion (although linear) between ice property estimation models and SAR data were investigated. Specifically, in work of Shi et al [14], issues arose near transition regions between sea ice and open sea water. Some potential directions of further research would be to incorporate information inferring the detection of these regions, whether that be through different image processing techniques on the SAR data, or through addition inputs, such as satellite images of these regions, in order to incorporate additional features into the estimation pipelines.

Using scattering models, such as an extended Bragg scattering model, was also investigated. Kim et al. work towards analyzing the correlation between the cross-polarization ratio and sea ice thickness for thick FYI and MYI. The results they provide are compelling, but rely on the assumption that surface roughness of this category of sea ice corresponds to sea ice thickness. This is not always the case, and is an assumption that should require further investigation.

Liu et al. explored the possibility of combining VIS/NIR images with SAR backscattering data for the purpose of ice thickness estimation. Due to the different properties of FYI and MYI, as well as level and rough ice, different sensing devices are more suited for measuring different stages of sea ice. They showed that using a combination of sensor modalities can lead to more effective estimates of ice properties. The results they show could benefit from CCD images taken at different angles, as they make heavy assumptions surrounding the reflective properties of the sea ice observed. The isotropic assumption of the physi-

cal structure of sea ice does not hold, and with the formulation of their reflectance values relying on this assumption, their estimates may suffer.

Comprehensive comparisons between different SAR frequency bands was also explored in the work of Howell et al. [3]. This work looked to quantify the previous theoretical assumptions surrounding the use of L-band SAR in the monitoring of sea ice, especially for estimating sea ice motion fields. The L-band SAR showed much more dense vector fields in almost all cases, with higher quality motion vectors. Since the goals for estimating sea ice drift require detecting detailed features of sea ice, the deeper penetration of L-band SAR helped with a lot of the challenges present with various ice surface non-uniformities. Penetrating through rough new ice surface and wet snow/water deposits on melting ice sheets aided in the formation of higher detailed backscatter images, ultimately leading to higher quality sea ice drift estimation.

The combination and fusion of both passive and active remote sensing for sea ice drift was explored by Girard-Ardhuin et al. Their work looked to fuse vector fields from both radiometers and scatterometers in order to compliment each sensing modality and produce a complete vector drift field over a several-day time window. In principle, this method works; however, relying on radiometer data that is unreliable in adverse weather conditions and without consistent radiation energy is sub-optimal.

It would be an interesting avenue of research to explore the possibility of incorporating different forms of optimization and machine learning into an ice properties estimation pipeline. Most of the previous work either relies on hand-selected image processing stages and feature extractions of SAR imagery, or the manual affine fusion of numerical models and remote sensing data in order to estimate different sea ice properties. With a more complex function approximation (through some form of learned regression model, or more advanced applications of deep learning), it may

be possible to produce more accurate estimations. The fusion of different sensing modalities seems to be a recurring topic in many of the works presented in this review. Merging sensor data taken from satellite images (visible and/or near-infrared), SAR backscattering measurements, numeric models, and local weather conditions into a unified pipeline as multi-channel vector inputs into such a function approximation may prove beneficial.

We provided in this work an introduction into the area of sea ice monitoring, providing some necessary background information, as well as motivation for the importance of this body of work. We introduce some of the technology that is primarily used in the field, along with the technical properties that make the sensing methods effective. We review several works residing in the sea ice monitoring realm, discussing their approaches and formulations, as well as any potential avenues of improvement.

References

[1] Fanny Girard-Ardhuin and Robert Ezraty. Enhanced Arctic Sea Ice Drift Estimation Merging Radiometer and Scatterometer Data. *IEEE Transactions on Geoscience and Remote Sensing*, 50(7):2639–2648, 2012. 1, 12, 13

[2] Irena Hajnsek, Eric Pottier, and Shane R Cloude. Inversion of surface parameters from polarimetric sar. *IEEE Transactions on Geoscience and Remote Sensing*, 41(4):727–744, 2003. 7

[3] Stephen EL Howell, Alexander S Komarov, Mohammed Dabboor, Benoit Montpetit, Michael Brady, Randall K Scharien, Mallik S Mahmud, Vishnu Nandan, Torsten Geldsetzer, and John J Yackel. Comparing L-and C-band synthetic aperture radar estimates of sea ice motion over different ice regimes. *Remote Sensing of Environment*, 204:380–391, 2018. 1, 10, 11, 12, 14

[4] Zhonghai Jin and James J Simpson. Bidirectional anisotropic reflectance of snow and sea ice in avhrr channel 1 and 2 spectral regions. i. theo-retical analysis. *IEEE transactions on geoscience and remote sensing*, 37(1):543–554, 1999. 10

[5] J. Karvonen, B. Cheng, T. Vihma, M. Arkett, and T. Carrieres. A method for sea ice thickness and concentration analysis based on sar data and a thermodynamic model. *The Cryosphere*, 6(6):1507–1526, 2012. 4, 5, 6

[6] Jin-Woo Kim, Duk-jin Kim, and Byong Jun Hwang. Estimation of sea ice thickness in the Arctic Sea using polarimetric parameters of C- and X-band space-borne SAR data. In *2010 IEEE International Geoscience and Remote Sensing Symposium*, pages 2402–2405, 2010. 1, 6, 7

[7] Alexander S Komarov and David G Barber. Sea ice motion tracking from sequential dual-polarization radarsat-2 images. *IEEE Transactions on Geoscience and Remote Sensing*, 52(1):121–136, 2013. 10, 11

[8] Chengyu Liu, Jinlong Chao, Wei Gu, Yingjun Xu, and Feng Xie. Estimation of sea ice thickness in the Bohai Sea using a combination of VIS/NIR and SAR images. *GIScience & Remote Sensing*, 52(2):115–130, 2015. 1, 8, 9

[9] Stuart Lloyd. Least squares quantization in pcm. *IEEE transactions on information theory*, 28(2):129–137, 1982. 5

[10] Alberto Moreira, Pau Prats-Iraola, Marwan Younis, Gerhard Krieger, Irena Hajnsek, and Konstantinos Papathanassiou. A tutorial on synthetic aperture radar. 10 2013. 4

[11] Kazuki Nakamura, Hiroyuki Wakabayashi, Kazuhiro Naoki, Fumihiko Nishio, et al. Sea-ice thickness retrieval in the sea of okhotsk using dual-polarization sar data. *Annals of Glaciology*, 44:261–268, 2006. 7

[12] Kazuki Nakamura, Hiroyuki Wakabayashi, Kazuhiro Naoki, Fumihiko Nishio, Teruo Moriyama, and Seiho Uratsuka. Observation of sea-ice thickness in the sea of okhotsk by using dual-frequency and fully polarimetric airborne sar (pi-sar) data. *IEEE Transactions on Geoscience and Remote Sensing*, 43(11):2460–2469, 2005. 7

[13] Robert G Onstott and FD Carsey. Sar and scatterometer signatures of sea ice. *Microwave remote sensing of sea ice*, 68:73–104, 1992. 2

[14] Shi, Lijian and Karvonen, Juha and Cheng, Bin and Vihma, Timo and Lin, Mingsen and Liu, Yu and Wang, Qimao and Jia, Yongjun. Sea ice thickness retrieval from sar imagery over bohai sea. In *2014 IEEE Geoscience and Remote Sensing Symposium*, pages 4864–4867. IEEE, 2014. 1, 4, 5, 14

[15] G. Spreen, L. Kaleschke, and G. Heygster. Sea ice remote sensing using amsr-e 89-ghz channels. *Journal of Geophysical Research: Oceans*, 113(C2), 2008. 5

[16] Praveen Rao Teleti and Alvarinho J Luis. Sea ice observations in polar regions: Evolution of technologies in remote sensing. 2013. 3

[17] W Tobler. Notes and comments on the composition of terrestrial and celestial maps, translation of jhl lambeck work, 1972. 5

[18] Leung Tsang, Jin Au Kong, and Kung-Hau Ding. *Scattering of electromagnetic waves: theories and applications*. John Wiley & Sons, 2004. 8

[19] Eric F Vermote, Didier Tanré, Jean L Deuze, Maurice Herman, and J-J Morcette. Second simulation of the satellite signal in the solar spectrum, 6s: An overview. *IEEE transactions on geoscience and remote sensing*, 35(3):675–686, 1997. 9

[20] Hiroyuki Wakabayashi, Takeshi Matsuoka, Kazuki Nakamura, and Fumihiko Nishio. Polarimetric characteristics of sea ice in the sea of okhotsk observed by airborne l-band sar. *IEEE Transactions on Geoscience and Remote Sensing*, 42(11):2412–2425, 2004. 7

[21] Pål Wessel and Walter HF Smith. A global, self-consistent, hierarchical, high-resolution shoreline database. *Journal of Geophysical Research: Solid Earth*, 101(B4):8741–8743, 1996. 5